ACS APPLIED MATERIALS & INTERFACES

www.acsami.org

Research Article

Point Defect Scattering and Phonon Softening for Achieving High Thermoelectric Performance in p-Type ZnSb with Optimal Carrier Concentration

Dongyi Shen, Siu Ting Tai, Kejia Liu, Wenxuan Wang, Haiqi Li, Vaskuri C. S. Theja, Chen Chen,* and Yue Chen*

Cite This: ACS Appl. Mater. Interfaces 2025, 17, 17036−17044

Read Online

ACCESS | Metrics & More | Article Recommendations | Supporting Information

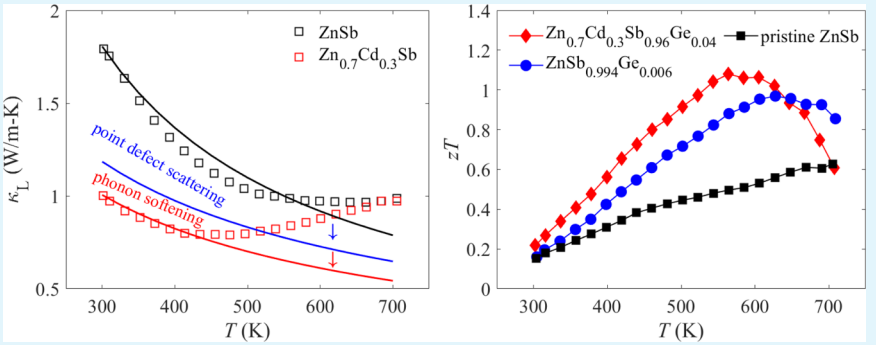

ABSTRACT: The thermoelectric material ZnSb has been intensively studied on account of its good thermodynamic stability and earth-abundant constituent elements, both of which make it feasible for mass production. However, the practical application of ZnSb is limited by its relatively poor thermoelectric performance, characterized by a low power factor and high lattice thermal conductivity. Herein, we demonstrate that there is a significant improvement in the thermoelectric figure of merit of ZnSb by combining Ge doping at the Sb site with Cd alloying at the Zn site. First, Ge doping at the Sb site can effectively optimize the carrier concentration, thereby resulting in an ∼82% increase in the peak power factor through a concentration of only 0.6%. Second, Cd alloying at the Zn site can bring about a strong point defect scattering to phonon propagation, leading to reduced phonon relaxation time. Meanwhile, the significant softening of acoustic phonons is also introduced by Cd alloying at the Zn site, and thus group velocities of acoustic phonon modes are suppressed. Consequently, a ∼44% reduction in the lattice thermal conductivity is achieved in $Zn_{0.7}Cd_{0.3}Sb$ at room temperature. As a result of the optimized carrier concentration and suppressed lattice thermal conductivity, a peak zT value as high as ∼1.08 at 564 K is attained in $Zn_{0.7}Cd_{0.3}Sb_{0.96}Ge_{0.04}$.

KEYWORDS: *thermoelectrics, zinc antimonide, point defect scattering, phonon softening, carrier concentration optimization*

INTRODUCTION

Global energy challenges and climate change lead to extensive research into thermoelectric (TE) materials, which are capable of recovering waste heat into electrical power without greenhouse gas emissions.[1−4] The energy conversion efficiency of TE materials depends on the dimensionless figure of merit $zT = S^2\sigma T/\kappa$, where S is the Seebeck coefficient, σ is the electrical conductivity, T is the absolute temperature, and κ is the total thermal conductivity generally comprising the electronic contribution κ_e and the lattice component κ_L.[5−7] The quantity $S^2\sigma$ is usually referred to as the power factor, which is associated with electrical transport properties. To achieve high-efficiency TE materials, we need to either enhance the power factor or suppress the thermal conductivity. Strategies for improving the power factor include carrier concentration optimization,[8,9] manipulation of carrier scattering mechanism,[10,11] and band structure engineering.[12,13] Efforts to reduce the thermal conductivity are mainly focused on decreasing the lattice component via phonon engineering because it is relatively independent of other thermoelectric parameters.[14,15] In recent years, high zT values have been discovered in chalcogenides,[16−18] half-Heusler alloys,[19,20] as well as Zintl-phase compounds[21−23] in consequence of relentless optimization.

Received: December 10, 2024
Revised: February 24, 2025
Accepted: February 25, 2025
Published: March 10, 2025

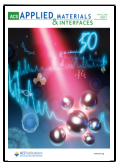

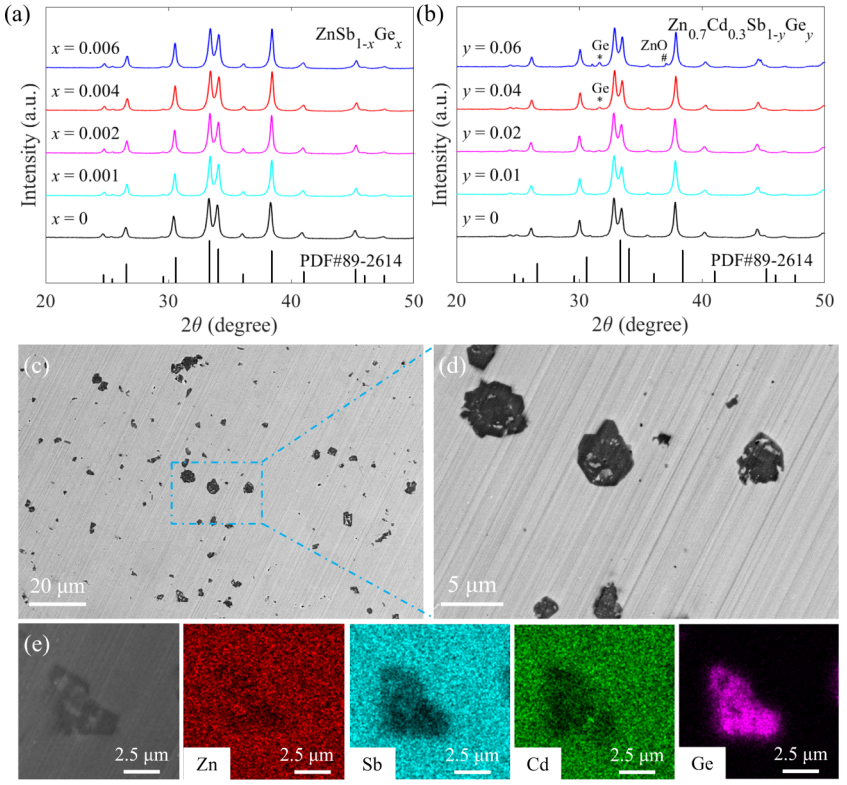

Figure 1. XRD patterns of (a) $ZnSb_{1-x}Ge_x$ (x = 0, 0.001, 0.002, 0.004, and 0.006) and (b) $Zn_{0.7}Cd_{0.3}Sb_{1-y}Ge_y$ (y = 0, 0.01, 0.02, 0.04, and 0.06) samples. BSE images of a polished surface for (c,d) $Zn_{0.7}Cd_{0.3}Sb_{0.96}Ge_{0.04}$. Elemental mappings of (e) Zn, Sb, Cd, and Ge for $Zn_{0.7}Cd_{0.3}Sb_{0.96}Ge_{0.04}$.

In addition to the aforementioned high-performance TE materials, zinc antimonides, typified by β-Zn_4Sb_3 and ZnSb, also attract much research attention because constituent elements are earth-abundant and relatively cheap. It is found that β-Zn_4Sb_3 has an intrinsically low lattice thermal conductivity of ~0.65 W m^{-1} K^{-1} at room temperature, which primarily arises from its complex crystal structure with disordered Zn atoms distributed among multiple interstitial sites.[24−27] High zT values above unity are achieved in p-type β-Zn_4Sb_3 after optimizing the carrier concentration by introducing various dopants.[28−30] However, the real-world application of β-Zn_4Sb_3 is severely impeded by its poor thermal stability under an electric field or a temperature gradient.[24,26,29] In contrast, ZnSb is much more stable than β-Zn_4Sb_3 when an electric field or a temperature gradient is applied. This is because all Zn atoms in ZnSb are orderly located at specific lattice sites.[24] From the perspective of thermodynamic stability, ZnSb is expected to be a promising alternative to β-Zn_4Sb_3, and many approaches are proposed to improve the TE performance of ZnSb.[24,31−35] Based on the density functional theory (DFT) calculations, it was predicted that substitution of Sb with Ge can effectively optimize the carrier concentration and thus enhance the zT value of ZnSb.[36] Since there is barely any experimental work to verify this theoretical prediction, it is necessary to explore the effect of Ge doping at the Sb site on the TE performance of ZnSb. Owing to the lack of interstitial Zn atoms, ZnSb has a higher room-temperature lattice thermal conductivity than β-Zn_4Sb_3. Although Cd alloying at the Zn site is commonly used to reduce the lattice thermal conductivity, its impact on the phonon propagation is seldom studied.[37−40]

In this work, we demonstrate that high TE performance in p-type ZnSb can be achieved through a combination of optimized carrier concentration and suppressed lattice thermal conductivity. First of all, Ge doping at the Sb site has been proven to be successful at optimizing the carrier concentration. Accordingly, the maximum power factor is remarkably improved from 11 μW cm^{-1} K^{-2} for pristine ZnSb at 705 K to 20 μW cm^{-1} K^{-2} for $ZnSb_{0.994}Ge_{0.006}$ at 480 K. Moreover, Cd alloying at the Zn site can dramatically suppress the lattice thermal conductivity to 1 W m^{-1} K^{-1} for $Zn_{0.7}Cd_{0.3}Sb$ from 1.79 W m^{-1} K^{-1} for pristine ZnSb at room temperature, which stems from point defect scattering and phonon softening. By combining Ge doping at the Sb site and Cd alloying at the Zn site together, a peak zT value as high as ~1.08 is attained in $Zn_{0.7}Cd_{0.3}Sb_{0.96}Ge_{0.04}$ at 564 K due to simultaneous optimization of the electrical and thermal transport properties. This suggests that ZnSb is a potential high-performance TE material.

EXPERIMENTAL SECTION

Sample Synthesis. According to the nominal compositions $ZnSb_{1-x}Ge_x$ (x = 0, 0.001, 0.002, 0.004, and 0.006) and $Zn_{0.7}Cd_{0.3}Sb_{1-y}Ge_y$ (y = 0, 0.01, 0.02, 0.04, and 0.06), stoichiometric amounts of constituent elements zinc (Zn, shots, 99.999%), antimony (Sb, shots, 99.99%), cadmium (Cd, shots, 99.999%), and germanium (Ge, pellets, 99.9999%) were weighed out and sealed in quartz tubes under vacuum. The quartz tubes were then heated to 1023 K and held at this temperature for 24 h followed by quenching in water. Subsequently, the quenched ingots were annealed at 573 K for 48 h before ball milling into fine powders. Finally, the fine powders were consolidated into dense pellets by hot pressing at 693 K for 5 min under a uniaxial pressure of 50 MPa.

Sample Characterization. The crystal structure was characterized on an X-ray diffractometer (Rigaku MiniFlex 600-C) with Co K_α radiation (λ = 1.7890 Å). The backscattered electron (BSE) imaging and elemental mapping were performed on the field emission

https://doi.org/10.1021/acsami.4c21670
ACS Appl. Mater. Interfaces 2025, 17, 17036−17044

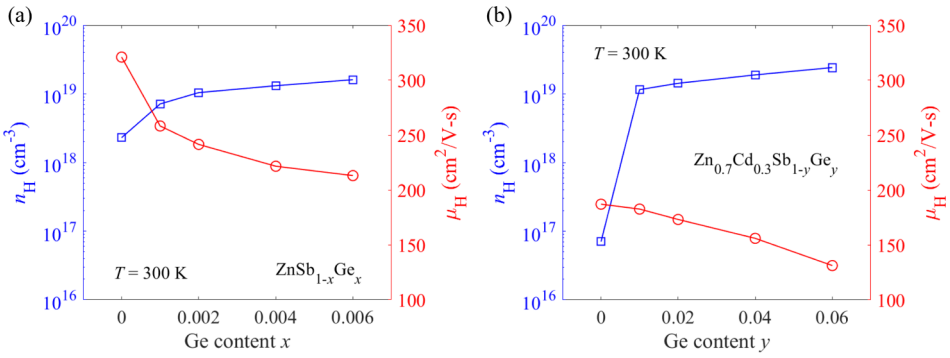

Figure 2. Room-temperature Hall carrier concentration and Hall mobility as a function of Ge content in (a) $ZnSb_{1-x}Ge_x$ (x = 0, 0.001, 0.002, 0.004, and 0.006) and (b) $Zn_{0.7}Cd_{0.3}Sb_{1-y}Ge_y$ (y = 0, 0.01, 0.02, 0.04, and 0.06) samples.

scanning electron microscope (FESEM, LEO 1530) equipped with an energy-dispersive X-ray spectrometer (EDS). The measurement of electrical transport properties was carried out in the low-pressure helium atmosphere. The electrical conductivity σ was measured using the van der Pauw technique.[41,42] The Hall coefficient R_H was determined by the Hall measurement under a reversible magnetic field of 1.5 T. The Hall carrier concentration n_H and Hall mobility μ_H were calculated from $n_H = 1/eR_H$ and $\mu_H = \sigma R_H$, respectively.[43] The Seebeck coefficient S was obtained from the slope of the Seebeck voltage versus temperature gradient in the temperature range of 0−5 K.[42] The thermal conductivity κ was derived from $\kappa = dC_p\alpha$, where d is the mass density determined by the Archimedes method, C_p is the isobaric specific heat estimated from the Dulong−Petit limit, and α is the thermal diffusivity measured on a laser flash analyzer (LFA1000, Linseis) in a flowing helium atmosphere.[44] The longitudinal ν_L and transverse ν_T sound velocities were gauged by using an ultrasonic pulse receiver (Olympus) equipped with an oscilloscope (Tektronix). The shear modulus G and bulk modulus B were calculated from the equations $\nu_T = (G/d)^{1/2}$ and $\nu_L = [(B + 4G/3)/d]^{1/2}$, respectively.

Computational Details. All DFT calculations were performed using projector-augmented wave (PAW) pseudopotentials and Perdew−Burke−Ernzerhof generalized gradient approximation (GGA-PBE) exchange-correlation functional in the Vienna Ab initio Simulation Package (VASP).[45,46] A plane-wave kinetic energy cutoff of 550 eV was used to truncate the basis in all DFT calculations. Geometry optimization was conducted on pristine ZnSb (eight Zn atoms and eight Sb atoms) and $Zn_{0.75}Cd_{0.25}Sb$, where doping was modeled by randomly substituting two Zn atoms with two Cd atoms. The composition ratio of $Zn_{0.75}Cd_{0.25}Sb$ was chosen in the computational model to maintain a reasonable supercell size for computational efficiency while keeping the doping concentration close to that of our experimental composition of $Zn_{0.7}Cd_{0.3}Sb$. All structures were fully relaxed until the forces and energies reached the convergence criteria of 1×10^{-4} eV/Å and 1×10^{-8} eV, respectively. A Γ-centered Monkhorst-Pack scheme k-point mesh of $6 \times 5 \times 5$ was adopted for the unit cell relaxation process, while the self-consistent force and energy calculations for phonon evaluation adopted a mesh of $3 \times 2 \times 2$ on the supercell model.[47] The electronic density of states (DOS) and band structure were evaluated using the modified Becke−Johnson (mBJ) potential, as it yields better agreement with experimental results.[48] Postprocessing of electronic structure data was carried out using the VASPKIT package for extraction of electronic DOS and band structure data.[49]

Calculations of harmonic phonon dispersion relation, DOS, and group velocity were performed using the Phonopy package.[50] $2 \times 2 \times 2$ supercells of pristine ZnSb and $Zn_{0.75}Cd_{0.25}Sb$ were employed in the finite displacement approach with a displacement amplitude of 0.01 Å to extract the second-order interatomic force constants of the systems.

RESULTS AND DISCUSSION

The X-ray diffraction (XRD) patterns of hot-pressed $ZnSb_{1-x}Ge_x$ (x = 0, 0.001, 0.002, 0.004, and 0.006) and $Zn_{0.7}Cd_{0.3}Sb_{1-y}Ge_y$ (y = 0, 0.01, 0.02, 0.04, and 0.06) samples are shown in Figure 1a and b, respectively. It is seen from Figure 1a that all diffraction peaks are well indexed to the ZnSb phase with an orthorhombic structure, and no obvious impurity peak is observed. This indicates that single-phase $ZnSb_{1-x}Ge_x$ (x = 0, 0.001, 0.002, 0.004, and 0.006) samples are successfully synthesized. For $Zn_{0.7}Cd_{0.3}Sb_{1-y}Ge_y$ (y = 0, 0.01, 0.02, 0.04, and 0.06) samples, as displayed in Figure 1b, all Bragg peaks show a systematic shift to the low-angle direction, which can be understood by the larger size of Cd than that of Zn. Moreover, when the Ge content reaches 0.04 and above, a secondary phase identified as Ge is detected. In addition to the Ge impurity phase, there is a small amount of ZnO in $Zn_{0.7}Cd_{0.3}Sb_{0.94}Ge_{0.06}$. The BSE images for a polished surface of hot-pressed $Zn_{0.7}Cd_{0.3}Sb_{0.96}Ge_{0.04}$ are presented in Figure 1c,d. As can be seen, numerous microscale precipitates are embedded in the matrix. According to elemental mapping results exhibited in Figure 1e, it is confirmed that the chemical composition of these microscale precipitates is Ge, which is in good agreement with XRD analysis.

Pristine ZnSb is intrinsically a p-type semiconductor on account of its native Zn vacancies.[24] It is seen from Figure 2a that the Hall carrier concentration of pristine ZnSb is 2.3×10^{18} cm^{-3} at room temperature, which is much lower than the optimal carrier concentration of 1.8×10^{19} cm^{-3}.[51] To increase the carrier concentration, Ge is chosen to substitute for Sb because Ge has one less valence electron than Sb. Furthermore, it is discovered that the formation energy of Ge_{Sb} substitutional defects is lower than that of Zn vacancies, which further shows the viability of Ge as an acceptor at the Sb site.[36] Consequently, it is found from Figure 2a that room-temperature Hall carrier concentration is increased to 1.6×10^{19} cm^{-3} when Ge content is 0.006, which is approximately seven times that of pristine ZnSb. In the meantime, Hall mobility decreases from 321 cm^2 V^{-1} s^{-1} for pristine ZnSb to 213 cm^2 V^{-1} s^{-1} for $ZnSb_{0.994}Ge_{0.006}$ at room temperature. After introducing Cd into the Zn site, room-temperature Hall carrier concentration sharply falls to 7.0×10^{16} cm^{-3}, and Hall mobility is simultaneously reduced to 187 cm^2 V^{-1} s^{-1} at 300 K, as displayed in Figure 2b. Given a dramatic decrease in Hall carrier concentration after Cd alloying at the Zn site, a significant decline in Hall mobility can be ascribed to the strong point defect scattering of charge carriers. Besides, our DFT calculations reveal that the band gap becomes slightly smaller after Cd alloying at the Zn site, as depicted in Figure S1. By further incorporating Ge into $Zn_{0.7}Cd_{0.3}Sb$, room-temperature Hall carrier concentration is increased by about 2

https://doi.org/10.1021/acsami.4c21670
ACS Appl. Mater. Interfaces 2025, 17, 17036−17044

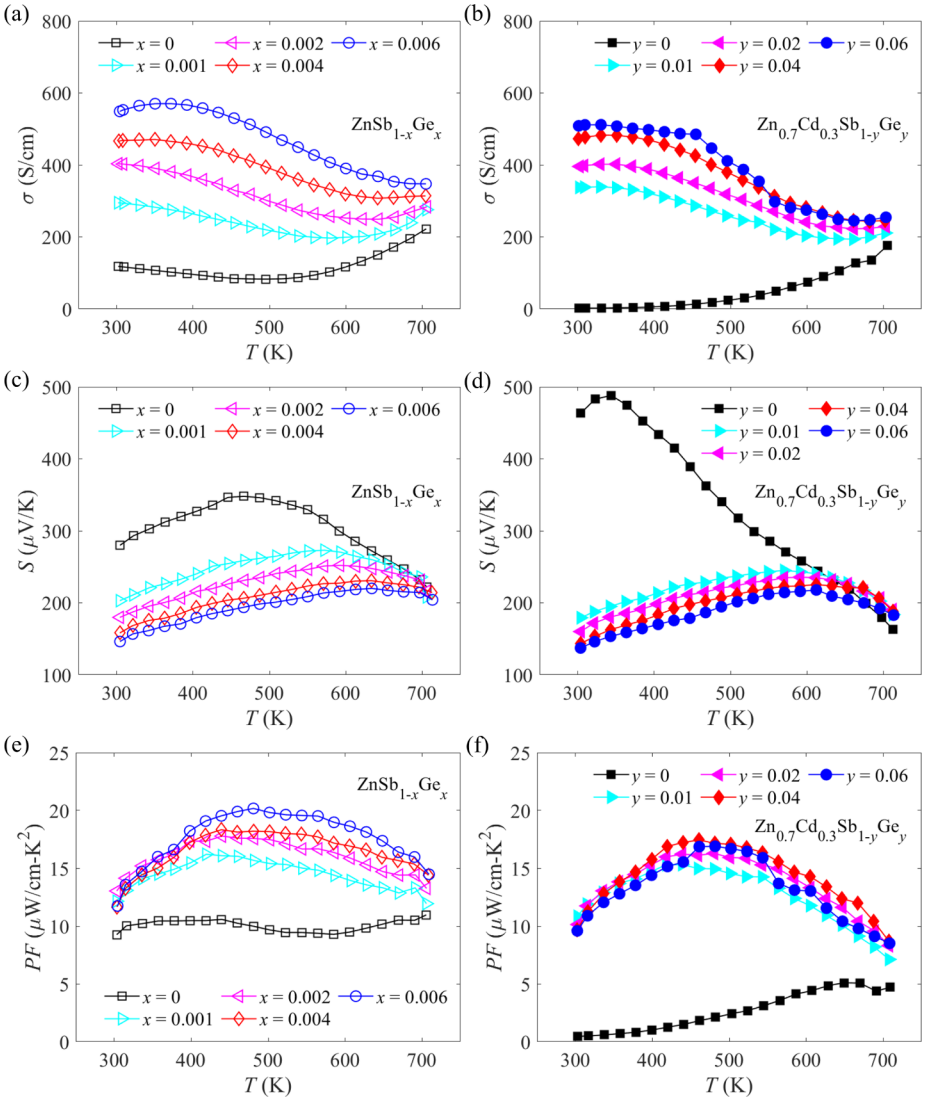

Figure 3. Temperature-dependent (a,b) electrical conductivities, (c,d) Seebeck coefficients, and (e,f) power factors of $ZnSb_{1-x}Ge_x$ (x = 0, 0.001, 0.002, 0.004, and 0.006) and $Zn_{0.7}Cd_{0.3}Sb_{1-y}Ge_y$ (y = 0, 0.01, 0.02, 0.04, and 0.06) samples.

orders of magnitude as opposed to that of $Zn_{0.7}Cd_{0.3}Sb$ and is eventually raised to 2.4×10^{19} cm^{-3} when Ge content is 0.06. This again implies that substitution of Sb with Ge is effective in tuning the carrier concentration over a broad range. According to Figure S2a,b, it is seen that Hall mobility of all samples decays with temperature approximately via $\mu_H \sim T^{-1.5}$ when temperature is above 450 K. This suggests that acoustic phonon scattering dominates the transport of charge carriers in this temperature range. However, when the temperature is below 400 K, the Hall mobility of Ge-doped $Zn_{0.7}Cd_{0.3}Sb$ samples is nearly independent of temperature, indicating that charge carriers in Ge-doped $Zn_{0.7}Cd_{0.3}Sb$ samples are mainly scattered by neutral impurities over this temperature range.

Temperature-dependent electrical transport properties for all samples are displayed in Figure 3. The electrical conductivity of $ZnSb_{1-x}Ge_x$ (x = 0, 0.001, 0.002, 0.004, and 0.006) and $Zn_{0.7}Cd_{0.3}Sb_{1-y}Ge_y$ (y = 0, 0.01, 0.02, 0.04, and 0.06) samples as a function of temperature is presented in Figure 3a and b, respectively. As a result of increased carrier concentration, the electrical conductivity is improved from 118 S cm^{-1} for pristine ZnSb to 549 S cm^{-1} for $ZnSb_{0.994}Ge_{0.006}$ at room temperature, as shown in Figure 3a. After incorporating Cd into the Zn site, room-temperature electrical conductivity drastically decreases to 2 S cm^{-1}, which can be attributed to the simultaneously reduced Hall carrier concentration and Hall mobility, as mentioned before. Additionally, the electrical conductivity of $Zn_{0.7}Cd_{0.3}Sb$ increases with increasing temperature across the entire temperature range, which can be seen as indicative of semiconducting behavior. However, this semiconducting behavior transforms to a nearly metallic behavior after the substitution of Sb with Ge in $Zn_{0.7}Cd_{0.3}Sb$. More importantly, with the addition of Ge to $Zn_{0.7}Cd_{0.3}Sb$, room-temperature electrical conductivity is enhanced by about 2 orders of magnitude as compared with that of $Zn_{0.7}Cd_{0.3}Sb$ and is finally increased to 509 S cm^{-1} when Ge content is 0.06.

The temperature dependences of Seebeck coefficients for $ZnSb_{1-x}Ge_x$ (x = 0, 0.001, 0.002, 0.004, and 0.006) and $Zn_{0.7}Cd_{0.3}Sb_{1-y}Ge_y$ (y = 0, 0.01, 0.02, 0.04, and 0.06) samples are exhibited in Figure 3c and d, respectively. A positive Seebeck coefficient indicates a p-type conduction for all samples, which is in compliance with the Hall measurement. Contrary to the variation of room-temperature electrical conductivity with Ge content, it is seen that the room-temperature Seebeck coefficient is reduced from 280 μV K^{-1}

https://doi.org/10.1021/acsami.4c21670
ACS Appl. Mater. Interfaces 2025, 17, 17036−17044

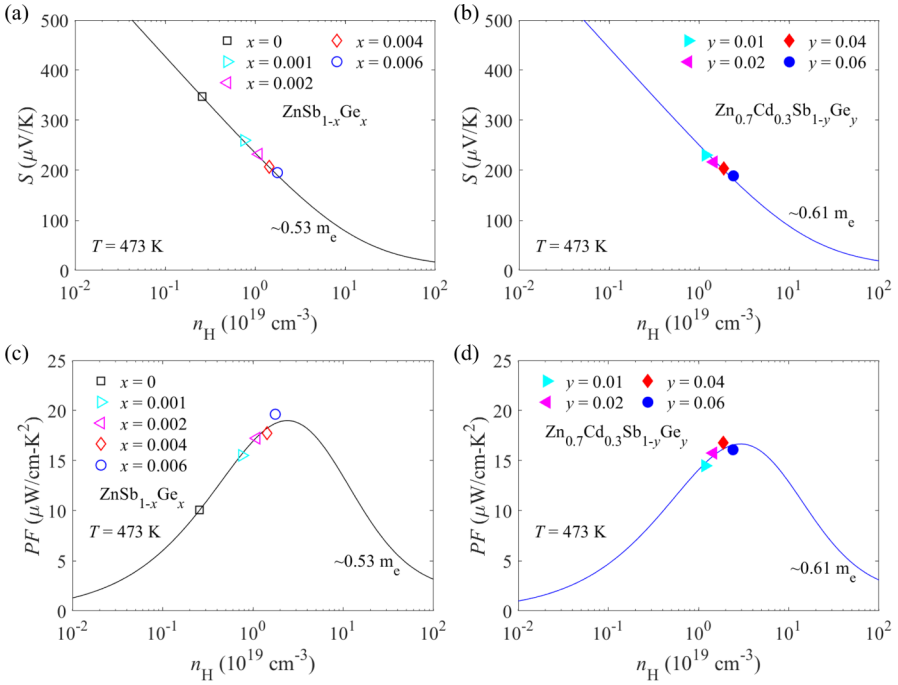

Figure 4. Hall carrier concentration-dependent (a,b) Seebeck coefficients and (c,d) power factors of $ZnSb_{1-x}Ge_x$ (x = 0, 0.001, 0.002, 0.004, and 0.006) and $Zn_{0.7}Cd_{0.3}Sb_{1-y}Ge_y$ (y = 0.01, 0.02, 0.04, and 0.06) samples at 473 K. The black and blue solid curves represent SPB models with DOS effective masses of ~0.53m_e and ~0.61m_e, respectively.

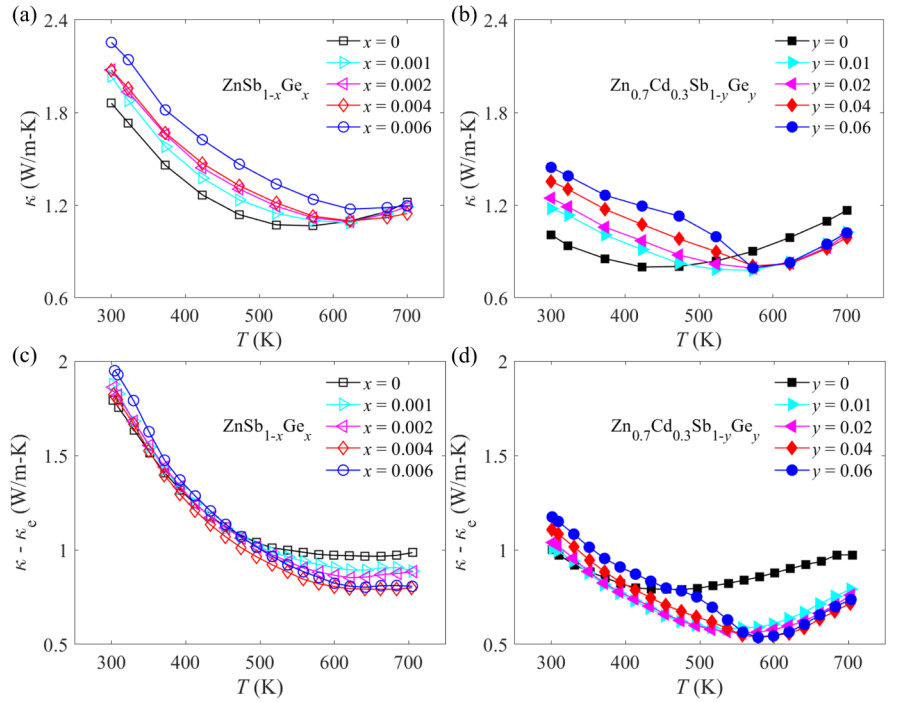

Figure 5. Temperature-dependent (a,b) thermal conductivities and (c,d) differences between total thermal conductivity and electronic thermal conductivity $\kappa-\kappa_e$ of $ZnSb_{1-x}Ge_x$ (x = 0, 0.001, 0.002, 0.004, and 0.006) and $Zn_{0.7}Cd_{0.3}Sb_{1-y}Ge_y$ (y = 0, 0.01, 0.02, 0.04, and 0.06) samples.

for pristine ZnSb to 146 μV K^{-1} for $ZnSb_{0.994}Ge_{0.006}$, and from 463 μV K^{-1} for $Zn_{0.7}Cd_{0.3}Sb$ to 137 μV K^{-1} for $Zn_{0.7}Cd_{0.3}Sb_{0.94}Ge_{0.06}$. The temperature-dependent power factors for $ZnSb_{1-x}Ge_x$ (x = 0, 0.001, 0.002, 0.004, and 0.006) and $Zn_{0.7}Cd_{0.3}Sb_{1-y}Ge_y$ (y = 0, 0.01, 0.02, 0.04, and 0.06) samples are illustrated in Figure 3e and f, respectively. It is seen from Figure 3e that the peak power factor is largely enhanced from 11 μW cm^{-1} K^{-2} for pristine ZnSb at 705 K to 20 μW cm^{-1} K^{-2} for $ZnSb_{0.994}Ge_{0.006}$ at 480 K. Nevertheless, Cd alloying at the Zn site is detrimental to the electrical transport properties because the power factor of $Zn_{0.7}Cd_{0.3}Sb$ is lower than that of pristine ZnSb over the entire temperature range. However, the substitution of Sb with Ge in $Zn_{0.7}Cd_{0.3}Sb$ can promote a noticeable recovery in the power factor, as depicted in Figure 3f.

https://doi.org/10.1021/acsami.4c21670
ACS Appl. Mater. Interfaces 2025, 17, 17036−17044

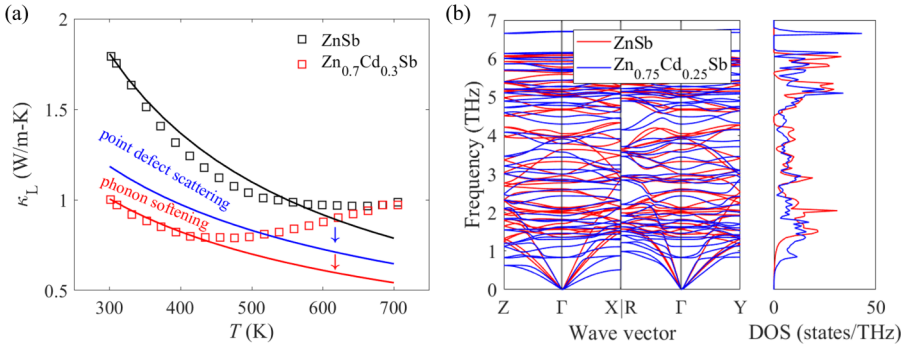

Figure 6. (a) Callaway-type model of lattice thermal conductivity under the Debye approximation. The reduction in κ_L from the black to blue curve is due to point defect scattering. The further reduction in κ_L from the blue to red curve is due to phonon softening. Experimental results for pristine ZnSb and $Zn_{0.7}Cd_{0.3}Sb$ are displayed in black and red squares, respectively. (b) The calculated phonon dispersion relations for pristine ZnSb and $Zn_{0.75}Cd_{0.25}Sb$ with the corresponding total phonon density of states (DOS).

The SPB model is utilized to gain more insights into the electrical transport properties of Ge-doped ZnSb and Ge-doped $Zn_{0.7}Cd_{0.3}Sb$ samples under the assumption that charge carriers are dominantly scattered by acoustic phonons at 473 K.[52−54] As shown in Figure 4a,b, the Pisarenko plot agrees well with our experimental results, which means that a trace amount of Ge has a limited effect on the DOS effective mass. Furthermore, it is found from Figure 4c,d that the theoretically predicted optimal carrier concentration for a maximum power factor at 473 K is achievable by adjusting the amount of Ge, suggesting that Ge is indeed a suitable dopant.

Temperature-dependent thermal transport properties for all samples are illustrated in Figure 5. The total thermal conductivity κ is typically the sum of lattice thermal conductivity κ_L and electronic thermal conductivity κ_e. However, it is reasonable to assume that the bipolar thermal conductivity κ_b is also included in the total thermal conductivity κ for this case because we notice that the total thermal conductivity for all samples appears to rise at high temperatures.[9,55] Furthermore, it is found from Figure 5a that the total thermal conductivity of Ge-doped ZnSb samples increases with increasing Ge content when the temperature ranges from 300 to 573 K. This is because of the enhanced electronic thermal conductivity, as shown in Figure S3a. A similar phenomenon can be observed in Ge-doped $Zn_{0.7}Cd_{0.3}Sb$ samples as well. The electronic thermal conductivity κ_e is proportional to the electrical conductivity through the Wiedemann−Franz relationship $\kappa_e = L\sigma T$, where L is the Lorenz number that can be derived from the measured Seebeck coefficient based on the SPB model.[55,56] The sum of the lattice thermal conductivity κ_L and the bipolar thermal conductivity κ_b can be estimated by subtracting the electronic part κ_e from the total thermal conductivity κ. Since bipolar thermal conductivity κ_b at 300 K is usually negligible, the room-temperature value of $\kappa-\kappa_e$ may be regarded as the lattice thermal conductivity κ_L.[57,58] It is seen from Figure 5c,d that the lattice thermal conductivity is largely reduced from 1.79 W m^{-1} K^{-1} for pristine ZnSb to 1 W m^{-1} K^{-1} for $Zn_{0.7}Cd_{0.3}Sb$ at room temperature. This indicates that Cd alloying at the Zn site is very effective in suppressing phonon propagation.

A Callaway-type model is constructed to elucidate the origin of the suppressed lattice thermal conductivity through Cd alloying at the Zn site. In the framework of this model, the lattice thermal conductivity can be expressed as follows:[59,60]

$$\kappa_L = \frac{1}{2\pi^2}\int_0^{k_{max}} c_{v,ph}(k, T)\tau_{tot}(k, T)v_g^2(k)k^2\,dk \quad (1)$$

Here, k_{max} stands for the maximum phonon wave vector obtained from $k_{max} = (6\pi^2/V_{avg})^{1/3}$, where V_{avg} is the average volume per atom. The heat capacity of a single-phonon mode $c_{v,ph}$ is given by $c_{v,ph} = k_B\frac{x^2e^x}{(e^x-1)^2}$ with $x = \hbar\omega/k_BT$, in which k_B is the Boltzmann constant, $\hbar$ is the reduced Planck constant, and ω is the phonon frequency. Based on Matthiessen's rule, the phonon relaxation time τ_{tot} can be calculated by considering the contributions from different scattering processes as follows:[19,20,61,62]

$$\tau_{tot}^{-1} = \sum_i \tau_i^{-1} \quad (2)$$

The phonon group velocity v_g is described as $v_g = \delta\omega/\delta k$. In the context of the Debye approximation, the phonon frequency ω is related to the phonon wave vector k via $\omega = v_s k$, where v_s denotes the average sound velocity. Therefore, the phonon group velocity in this model is identical to the average sound velocity under the Debye approximation. To unveil the role of point defect scattering in thermal transport, we calculate the phonon relaxation time for pristine ZnSb and $Zn_{0.7}Cd_{0.3}Sb$ separately while the average sound velocity remains unchanged. Only Umklapp scattering, normal scattering, and grain boundary scattering are taken into consideration when evaluating the phonon relaxation time for pristine ZnSb, whereas point defect scattering as an extra source of thermal resistance is included in the case of $Zn_{0.7}Cd_{0.3}Sb$. As shown in Figure 6a, point defect scattering can result in a large decrease in the lattice thermal conductivity, especially at room temperature. This is due to mass and strain-field fluctuations caused by differences in atomic mass and size between Zn and Cd atoms.[17,63] However, it is worth noting that such a drastic reduction in room-temperature lattice thermal conductivity can only be partly accounted for by point defect scattering. The results of sound velocity measurements as well as shear and bulk moduli for pristine ZnSb and $Zn_{0.7}Cd_{0.3}Sb$ are listed in Table 1. Evidently, the drop in sound velocities and moduli after Cd alloying at the Zn site is a robust indicator of phonon softening. This necessitates the incorporation of phonon softening into this model to uncover its effect on thermal transport. After replacing the average sound velocity of pristine ZnSb with that of $Zn_{0.7}Cd_{0.3}Sb$, a further decrease in the lattice thermal conductivity, which is induced by phonon softening, is

https://doi.org/10.1021/acsami.4c21670
ACS Appl. Mater. Interfaces 2025, 17, 17036−17044

Table 1. Longitudinal Sound Velocity ν_L, Transverse Sound Velocity ν_T, Average Sound Velocity ν_s, Shear Modulus G, and Bulk Modulus B for Pristine ZnSb and $Zn_{0.7}Cd_{0.3}Sb$ at Room Temperature

Sample	ν_L (m s^{-1})	ν_T (m s^{-1})	ν_s (m s^{-1})	G (GPa)	B (GPa)
Pristine ZnSb	4088	2206	2462	30.6	64.4
$Zn_{0.7}Cd_{0.3}Sb$	3744	2038	2273	26.9	54.9

observed.[59,64] It is noted that the discrepancy in the lattice thermal conductivity between experimental results and theoretical prediction at elevated temperatures can be explained by bipolar diffusion. To develop a deeper understanding of phonon softening, the phonon dispersion relations and phonon DOS for pristine ZnSb and $Zn_{0.75}Cd_{0.25}Sb$ are calculated (Figure 6b). As can be seen, Cd alloying at the Zn site introduces low-frequency optical phonons at ~1 THz and leads to the softening of acoustic phonons. The calculated group velocities of acoustic phonon modes for pristine ZnSb and $Zn_{0.75}Cd_{0.25}Sb$ near the Γ point are listed in Table 2, which

Table 2. Calculated Group Velocities (m s^{-1}) of Acoustic Phonon Modes for Pristine ZnSb and $Zn_{0.75}Cd_{0.25}Sb$ near the Γ Point

	Pristine ZnSb		$Zn_{0.75}Cd_{0.25}Sb$	
	Γ−Z	Γ−X	Γ−Z	Γ−X
TA	2439	2326	1585	1737
TA′	2841	2562	2108	2261
LA	4227	3987	4118	3823

are consistent with the results of the sound velocity measurement listed in Table 1. Our findings show that Cd alloying at the Zn site can not only reduce the phonon relaxation time but also decrease the group velocity of acoustic phonon modes, leading to the suppressed lattice thermal conductivity.

The temperature dependence of zT values for all samples is shown in Figure 7. The peak zT value of pristine ZnSb is ~0.63 at 700 K. Benefiting from remarkable improvement in power factor and significant suppression of lattice thermal conductivity, the peak zT value is enhanced to ~1.08 at 564 K for $Zn_{0.7}Cd_{0.3}Sb_{0.96}Ge_{0.04}$. It can be seen from Figure 7a,b that the peak zT value achieved in this work is comparable to those previously reported for other ZnSb-based thermoelectric materials.

CONCLUSION

In summary, TE properties of p-type $ZnSb_{1-x}Ge_x$ (x = 0, 0.001, 0.002, 0.004, and 0.006) and $Zn_{0.7}Cd_{0.3}Sb_{1-y}Ge_y$ (y = 0, 0.01, 0.02, 0.04, and 0.06) samples are thoroughly investigated in this work. Ge doping at the Sb site can enable carrier concentration optimization and thus considerable enhancement of the electrical transport properties. In addition, Cd alloying at the Zn site can significantly suppress the lattice thermal conductivity owing to point defect scattering and phonon softening. By virtue of a synergistic improvement in electrical and thermal transport properties, a peak zT value of ~1.08 is achieved in $Zn_{0.7}Cd_{0.3}Sb_{0.96}Ge_{0.04}$ at 564 K, confirming that ZnSb is a promising TE material.

ASSOCIATED CONTENT

Supporting Information

The Supporting Information is available free of charge at https://pubs.acs.org/doi/10.1021/acsami.4c21670.

Calculation of phonon relaxation time for pristine ZnSb and $Zn_{0.7}Cd_{0.3}Sb$; actual chemical compositions of Ge-doped $Zn_{0.7}Cd_{0.3}Sb$ samples; electronic band structures and densities of states (DOS) for pristine ZnSb and $Zn_{0.75}Cd_{0.25}Sb$; temperature-dependent Hall mobility and electronic thermal conductivity for all samples (PDF)

AUTHOR INFORMATION

Corresponding Authors

Chen Chen − *School of Physical Sciences, Great Bay University, Dongguan, Guangdong 523000, China*; Email: ccmldn@gbu.edu.cn

Yue Chen − *Department of Mechanical Engineering, The University of Hong Kong, Hong Kong SAR, China*; Email: yuechen@hku.hk

Authors

Dongyi Shen − *Department of Mechanical Engineering, The University of Hong Kong, Hong Kong SAR, China*; orcid.org/0009-0004-3245-0396

Siu Ting Tai − *Department of Mechanical Engineering, The University of Hong Kong, Hong Kong SAR, China*; orcid.org/0009-0000-2571-1317

Kejia Liu − *Department of Mechanical Engineering, The University of Hong Kong, Hong Kong SAR, China*

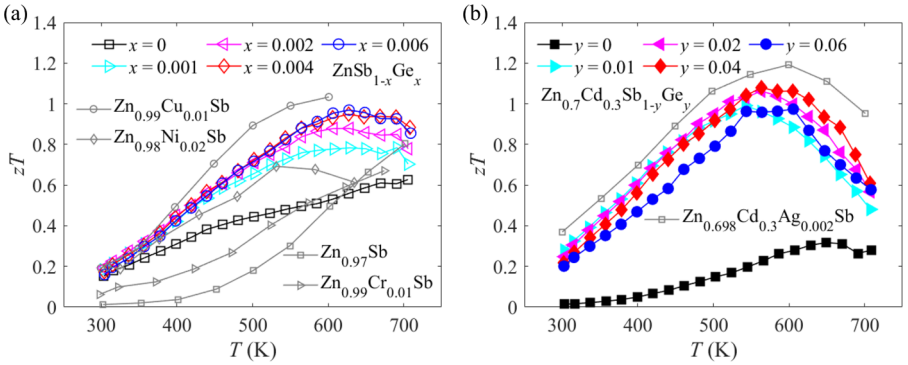

Figure 7. Temperature-dependent zT values of (a) $ZnSb_{1-x}Ge_x$ (x = 0, 0.001, 0.002, 0.004, and 0.006) and (b) $Zn_{0.7}Cd_{0.3}Sb_{1-y}Ge_y$ (y = 0, 0.01, 0.02, 0.04, and 0.06) samples. zT values previously reported for other ZnSb-based thermoelectric materials are included for comparison.[24,31,65−67]

https://doi.org/10.1021/acsami.4c21670
ACS Appl. Mater. Interfaces 2025, 17, 17036−17044

Wenxuan Wang − *Department of Mechanical Engineering, The University of Hong Kong, Hong Kong SAR, China;* orcid.org/0000-0002-4893-8618
Haiqi Li − *Department of Mechanical Engineering, The University of Hong Kong, Hong Kong SAR, China*
Vaskuri C. S. Theja − *Department of Mechanical Engineering, The University of Hong Kong, Hong Kong SAR, China*

Complete contact information is available at: https://pubs.acs.org/10.1021/acsami.4c21670

Notes

The authors declare no competing financial interest.

■ ACKNOWLEDGMENTS

This work is supported by the Guangdong Major Project of Basic and Applied Basic Research (2020B0301030001) and the Research Grants Council of Hong Kong (C7002-22Y, 17318122, and C6020-22GF). The authors are grateful for the research computing facilities offered by ITS, HKU.

■ REFERENCES

(1) Bell, L. E. Cooling, heating, generating power, and recovering waste heat with thermoelectric systems. *Science* **2008**, *321* (5895), 1457−1461.
(2) DiSalvo, F. J. Thermoelectric cooling and power generation. *Science* **1999**, *285* (5428), 703−706.
(3) Yang, J.; Caillat, T. Thermoelectric materials for space and automotive power generation. *MRS Bull.* **2006**, *31* (3), 224−229.
(4) Bu, Z.; Zhang, X.; Hu, Y.; Chen, Z.; Lin, S.; Li, W.; Xiao, C.; Pei, Y. A record thermoelectric efficiency in tellurium-free modules for low-grade waste heat recovery. *Nat. Commun.* **2022**, *13* (1), 237.
(5) Snyder, G. J.; Toberer, E. S. Complex thermoelectric materials. *Nat. Mater.* **2008**, *7* (2), 105−114.
(6) Tan, G.; Zhao, L.-D.; Kanatzidis, M. G. Rationally designing high-performance bulk thermoelectric materials. *Chem. Rev.* **2016**, *116* (19), 12123−12149.
(7) Zhu, T.; Liu, Y.; Fu, C.; Heremans, J. P.; Snyder, J. G.; Zhao, X. Compromise and synergy in high-efficiency thermoelectric materials. *Adv. Mater.* **2017**, *29* (14), 1605884.
(8) Wang, S.; Zhang, L.; Hong, T.; Su, L.; Wen, Y.; Qin, B.; Xiao, Y.; Wang, Y.; Shi, H.; Zheng, J.; Qiu, Y.; et al. Realizing remarkable improvement of electrical performance in n-type $BiSbSe_3$ via in situ compositing. *Adv. Funct. Mater.* **2024**, *34* (4), 2310335.
(9) Shen, D.; Cheng, R.; Wang, W.; Li, H.; Chen, C.; Zhang, Q.; Chen, Y. Enhanced thermoelectric performance of p-type $Bi_2Si_2Te_6$ enabled via synergistically optimizing carrier concentration and suppressing bipolar effect. *Mater. Today Phys.* **2023**, *37*, 101185.
(10) Mao, J.; Shuai, J.; Song, S.; Wu, Y.; Dally, R.; Zhou, J.; Liu, Z.; Sun, J.; Zhang, Q.; Dela Cruz, C.; Wilson, S.; et al. Manipulation of ionized impurity scattering for achieving high thermoelectric performance in n-type Mg_3Sb_2-based materials. *Proc. Natl. Acad. Sci. U. S. A.* **2017**, *114* (40), 10548−10553.
(11) Shuai, J.; Mao, J.; Song, S.; Zhu, Q.; Sun, J.; Wang, Y.; He, R.; Zhou, J.; Chen, G.; Singh, D. J.; et al. Tuning the carrier scattering mechanism to effectively improve the thermoelectric properties. *Energy Environ. Sci.* **2017**, *10* (3), 799−807.
(12) Tang, J.; Yao, Z.; Chen, Z.; Lin, S.; Zhang, X.; Xiong, F.; Li, W.; Chen, Y.; Pei, Y. Maximization of transporting bands for high-performance SnTe alloy thermoelectrics. *Mater. Today Phys.* **2019**, *9*, 100091.
(13) Tang, J.; Gao, B.; Lin, S.; Li, J.; Chen, Z.; Xiong, F.; Li, W.; Chen, Y.; Pei, Y. Manipulation of band structure and interstitial defects for improving thermoelectric SnTe. *Adv. Funct. Mater.* **2018**, *28* (34), 1803586.
(14) Zhang, Z.; Yao, H.; Wang, Q.; Xue, W.; Wang, Y.; Yin, L.; Wang, X.; Li, X.; Chen, C.; Sui, J.; Lin, X.; et al. Achieving high thermoelectric performance in severely distorted $YbCd_2Sb_2$. *Adv. Funct. Mater.* **2022**, *32* (35), 2205215.
(15) Yang, J.; Zhang, W.; Bai, S. Q.; Mei, Z.; Chen, L. D. Dual-frequency resonant phonon scattering in $Ba_xR_yCo_4Sb_{12}$ (R= La, Ce, and Sr). *Appl. Phys. Lett.* **2007**, *90* (19), 192111.
(16) Bu, Z.; Zhang, X.; Shan, B.; Tang, J.; Liu, H.; Chen, Z.; Lin, S.; Li, W.; Pei, Y. Realizing a 14% single-leg thermoelectric efficiency in GeTe alloys. *Sci. Adv.* **2021**, *7* (19), No. eabf2738.
(17) Wang, X.; Yao, H.; Yin, L.; Xue, W.; Zhang, Z.; Duan, S.; Chen, L.; Chen, C.; Sui, J.; Liu, X.; Wang, Y.; et al. Band modulation and strain fluctuation for realizing high average zT in GeTe. *Adv. Energy Mater.* **2022**, *12* (26), 2201043.
(18) Wu, Y.; Nan, P.; Chen, Z.; Zeng, Z.; Liu, R.; Dong, H.; Xie, L.; Xiao, Y.; Chen, Z.; Gu, H.; Li, W.; et al. Thermoelectric enhancements in PbTe alloys due to dislocation-induced strains and converged bands. *Adv. Sci.* **2020**, *7* (12), 1902628.
(19) Xie, H.; Wang, H.; Pei, Y.; Fu, C.; Liu, X.; Snyder, G. J.; Zhao, X.; Zhu, T. Beneficial contribution of alloy disorder to electron and phonon transport in half-Heusler thermoelectric materials. *Adv. Funct. Mater.* **2013**, *23* (41), 5123−5130.
(20) He, R.; Zhu, T.; Wang, Y.; Wolff, U.; Jaud, J.-C.; Sotnikov, A.; Potapov, P.; Wolf, D.; Ying, P.; Wood, M.; Liu, Z. Unveiling the phonon scattering mechanisms in half-Heusler thermoelectric compounds. *Energy Environ. Sci.* **2020**, *13* (12), 5165−5176.
(21) Tang, J.; Qin, C.; Yu, H.; Zeng, Z.; Cheng, L.; Ge, B.; Chen, Y.; Li, W.; Pei, Y. Ultralow lattice thermal conductivity enables high thermoelectric performance in $BaAg_2Te_2$ alloys. *Mater. Today Phys* **2022**, *22*, 100591.
(22) Zhang, Z.; Yan, Y.; Li, X.; Wang, X.; Li, J.; Chen, C.; Cao, F.; Sui, J.; Lin, X.; Liu, X.; Xie, G.; et al. A dual role by incorporation of magnesium in $YbZn_2Sb_2$ Zintl phase for enhanced thermoelectric performance. *Adv. Energy Mater.* **2020**, *10* (29), 2001229.
(23) Jiang, F.; Feng, T.; Zhu, Y.; Han, Z.; Shu, R.; Chen, C.; Zhang, Y.; Xia, C.; Wu, X.; Yu, H.; Liu, C.; et al. Extraordinary thermoelectric performance, thermal stability and mechanical properties of n-type $Mg_3Sb_{1.5}Bi_{0.5}$ through multi-dopants at interstitial site. *Mater. Today Phys.* **2022**, *27*, 100835.
(24) Yang, S.; Deng, T.; Qiu, P.; Xing, T.; Cheng, J.; Jin, Z.; Li, P.; Shi, X.; Chen, L. High-performance and stable (Ag, Cd)-containing ZnSb thermoelectric compounds. *ACS Appl. Mater. Interfaces* **2022**, *14* (23), 26662−26670.
(25) Snyder, G. J.; Christensen, M.; Nishibori, E.; Caillat, T.; Iversen, B. B. Disordered zinc in Zn_4Sb_3 with phonon-glass and electron-crystal thermoelectric properties. *Nat. Mater.* **2004**, *3* (7), 458−463.
(26) Yang, D.; Su, X.; He, J.; Yan, Y.; Li, J.; Bai, H.; Luo, T.; Liu, Y.; Luo, H.; Yu, Y.; Wu, J.; et al. Fast ion transport for synthesis and stabilization of β-Zn_4Sb_3. *Nat. Commun.* **2021**, *12* (1), 6077.
(27) Caillat, T.; Fleurial, J.-P.; Borshchevsky, A. Preparation and thermoelectric properties of semiconducting Zn_4Sb_3. *J. Phys. Chem. Solids* **1997**, *58* (7), 1119−1125.
(28) Li, D.; Hng, H.; Ma, J.; Qin, X. Effects of Nb doping on thermoelectric properties of Zn_4Sb_3 at high temperatures. *J. Mater. Res.* **2009**, *24* (2), 430−435.
(29) Zheng, J.; Tang, Y.; Shen, K.; Shen, L.; Ge, W.; Yang, P.; Deng, S. Low thermal conductivity and enhancement in figure-of-merit in Na and Mg co-doped β-Zn_4Sb_3. *J. Electron. Mater.* **2023**, *52* (1), 559−568.
(30) Liu, M.; Qin, X.; Liu, C.; Pan, L.; Xin, H. Ag and Cu doping and their effects on the thermoelectric properties of β-Zn_4Sb_3. *Phys. Rev. B* **2010**, *81* (24), 245215.
(31) Guo, Q.; Luo, S. Improved thermoelectric efficiency in p-type ZnSb through Zn deficiency. *Funct. Mater. Lett.* **2015**, *8* (2), 1550028.
(32) Valset, K.; Song, X.; Finstad, T. G. A study of transport properties in Cu and P doped ZnSb. *J. Appl. Phys.* **2015**, *117* (4), 045709.
(33) Prokofieva, L.; Konstantinov, P.; Shabaldin, A.; Pshenai-Severin, D.; Burkov, A.; Fedorov, M. Doping and defect formation in

thermoelectric ZnSb doped with copper. *Semiconductors* **2014**, *48*, 1571−1580.
(34) Böttger, P. M.; Pomrehn, G. S.; Snyder, G. J.; Finstad, T. G. Doping of p-type ZnSb: single parabolic band model and impurity band conduction. *Phys. Status Solidi A* **2011**, *208* (12), 2753−2759.
(35) Xiong, D.-B.; Okamoto, N. L.; Inui, H. Enhanced thermoelectric figure of merit in p-type Ag-doped ZnSb nanostructured with Ag_3Sb. *Scr. Mater.* **2013**, *69* (5), 397−400.
(36) Berche, A.; Jund, P. Thermoelectric power factor of pure and doped ZnSb via DFT based defect calculations. *Phys. Chem. Chem. Phys.* **2019**, *21* (41), 23056−23064.
(37) Liu, Y.; Tedenac, J.-C. Thermodynamic modeling of the Cd−Sb−Zn ternary system. *Calphad* **2009**, *33* (4), 684−694.
(38) Record, M.; Izard, V.; Bulanova, M.; Tedenac, J. Phase transformations in the Zn−Cd−Sb system. *Intermetallics* **2003**, *11* (11−12), 1189−1194.
(39) Biswas, R.; Patro, P. K.; Dasgupta, T. Enhanced thermoelectric performance in $Zn_{1-x}Cd_xSb$ (x = 0−0.375) solid solutions by dynamic optimization of charge carrier concentration. *ACS Appl. Energy Mater.* **2022**, *5* (10), 12752−12759.
(40) Biswas, R.; Mukherjee, S.; Mallik, R.; Vitta, S.; Dasgupta, T. Ultralow thermal conductivity and low charge carrier scattering potential in $Zn_{1-x}Cd_xSb$ solid solutions for thermoelectric application. *Mater. Today Energy* **2019**, *12*, 107−113.
(41) van der Pauw, L. J. A method of measuring specific resistivity and Hall effect of discs of arbitrary shape. *Philips Research Reports* **1958**, *13* (1), 1−9.
(42) Zhou, Z.; Uher, C. Apparatus for Seebeck coefficient and electrical resistivity measurements of bulk thermoelectric materials at high temperature. *Rev. Sci. Instrum.* **2005**, *76* (2), 023901.
(43) Green, R.Hall effect measurements in materials characterization*White Paper*20113111
(44) Parker, W.; Jenkins, R.; Butler, C.; Abbott, G. Flash method of determining thermal diffusivity, heat capacity, and thermal conductivity. *J. Appl. Phys.* **1961**, *32* (9), 1679−1684.
(45) Blöchl, P. E. Projector augmented-wave method. *Phys. Rev. B* **1994**, *50* (24), 17953.
(46) Perdew, J. P.; Burke, K.; Ernzerhof, M. Generalized gradient approximation made simple. *Phys. Rev. Lett.* **1996**, *77* (18), 3865.
(47) Monkhorst, H. J.; Pack, J. D. Special points for Brillouin-zone integrations. *Phys. Rev. B* **1976**, *13* (12), 5188.
(48) Tran, F.; Blaha, P. Accurate Band Gaps of Semiconductors and Insulators with a Semilocal Exchange-Correlation Potential. *Phys. Rev. Lett.* **2009**, *102* (22), 226401.
(49) Wang, V.; Xu, N.; Liu, J.-C.; Tang, G.; Geng, W.-T. VASPKIT: A user-friendly interface facilitating high-throughput computing and analysis using VASP code. *Comput. Phys. Commun.* **2021**, *267*, 108033.
(50) Togo, A. First-principles phonon calculations with phonopy and phono3py. *J. Phys. Soc. Jpn.* **2023**, *92* (1), 012001.
(51) Wood, M.; Toriyama, M. Y.; Dugar, S.; Male, J.; Anand, S.; Stevanović, V.; Snyder, G. J. Phase boundary mapping of tin-doped ZnSb reveals thermodynamic route to high thermoelectric efficiency. *Adv. Energy Mater.* **2021**, *11* (20), 2100181.
(52) Zhao, L.-D.; Lo, S.-H.; He, J.; Li, H.; Biswas, K.; Androulakis, J.; Wu, C.-I.; Hogan, T. P.; Chung, D.-Y.; Dravid, V. P.; Kanatzidis, M. G. High performance thermoelectrics from earth-abundant materials: enhanced figure of merit in PbS by second phase nanostructures. *J. Am. Chem. Soc.* **2011**, *133* (50), 20476−20487.
(53) Naithani, H.; Dasgupta, T. Critical analysis of single band modeling of thermoelectric materials. *ACS Appl. Energy Mater.* **2020**, *3* (3), 2200−2213.
(54) Zhu, J.; Zhang, X.; Guo, M.; Li, J.; Hu, J.; Cai, S.; Cai, W.; Zhang, Y.; Sui, J. Restructured single parabolic band model for quick analysis in thermoelectricity. *Npj Comput. Mater.* **2021**, *7* (1), 116.
(55) May, A. F.; Snyder, G. J.Introduction to modeling thermoelectric transport at high temperatures*Materials, Preparation, And Characterization In Thermoelectrics*CRC Press20121−18
(56) Kim, H.-S.; Gibbs, Z. M.; Tang, Y.; Wang, H.; Snyder, G. J. Characterization of Lorenz number with Seebeck coefficient measurement. *APL Mater.* **2015**, *3* (4), 041506.
(57) Xiao, Y.; Wu, H.; Cui, J.; Wang, D.; Fu, L.; Zhang, Y.; Chen, Y.; He, J.; Pennycook, S. J.; Zhao, L.-D. Realizing high performance n-type PbTe by synergistically optimizing effective mass and carrier mobility and suppressing bipolar thermal conductivity. *Energy Environ. Sci.* **2018**, *11* (9), 2486−2495.
(58) Wu, X.; Wang, Z.; Jiang, R.; Tian, Y.; Liu, Y.; Shi, J.; Zhao, W.; Xiong, R. Enhanced thermoelectric performance of p-type Bi_2Te_3-based materials by suppressing bipolar thermal conductivity. *Mater. Today Phys.* **2022**, *29*, 100904.
(59) Tan, G.; Hao, S.; Hanus, R. C.; Zhang, X.; Anand, S.; Bailey, T. P.; Rettie, A. J. E.; Su, X.; Uher, C.; Dravid, V. P.; Snyder, G. J.; et al. High Thermoelectric Performance in SnTe−$AgSbTe_2$ Alloys from Lattice Softening, Giant Phonon−Vacancy Scattering, and Valence Band Convergence. *ACS Energy Lett.* **2018**, *3* (3), 705−712.
(60) Callaway, J. Model for lattice thermal conductivity at low temperatures. *Phys. Rev.* **1959**, *113* (4), 1046.
(61) Hu, C.; Xia, K.; Chen, X.; Zhao, X.; Zhu, T. Transport mechanisms and property optimization of p-type (Zr, Hf) CoSb half-Heusler thermoelectric materials. *Mater. Today Phys.* **2018**, *7*, 69−76.
(62) Zhu, J.; Tan, X.; Pan, D.; Luo, Y.; Li, R.; Rao, X.; Cheng, R.; Xia, C.; Chen, Y.; Sun, Q.; Ang, R. Functionally separated electronic band engineering via multi-element doping plus high-density defects advances board-temperature-range thermoelectric performance in GeTe. *Chem. Eng. J.* **2024**, *480*, 148135.
(63) Chen, C.; Shen, D.; Xia, C.; Zhang, Z.; Wang, W.; Zhang, Q.; Chen, Y. Integrating band engineering with point defect scattering for high thermoelectric performance in $Bi_2Si_2Te_6$. *Chem. Eng. J.* **2022**, *441*, 135968.
(64) Han, S.; Dai, S.; Ma, J.; Ren, Q.; Hu, C.; Gao, Z.; Duc Le, M.; Sheptyakov, D.; Miao, P.; Torii, S.; Kamiyama, T.; et al. Strong phonon softening and avoided crossing in aliovalence-doped heavy-band thermoelectrics. *Nat. Phys.* **2023**, *19* (11), 1649−1657.
(65) Kang, S. H.; Heo, M.; Jung, Y.-J.; Lee, J. M.; Jeong, C.; Koo, S.-M.; Nam, W. H.; Cho, J. Y.; Lee, K. H.; Kim, H.-S.; Shin, W. H. Enhanced thermoelectric performance of Cr-doped ZnSb through lattice thermal conductivity reduction below the phonon glass limit. *J. Alloy. Compd.* **2024**, *1002*, 175402.
(66) Dharmaiah, P.; Heo, M.; Nagarjuna, C.; Jung, S.-J.; Won, S. O.; Lee, K. H.; Kim, S. K.; Kim, J.-S.; Ahn, B.; Kim, H.-S.; Baek, S.-H. Enhancement of thermoelectric properties in p-type ZnSb alloys through Cu-doping. *J. Alloy. Compd.* **2024**, *1004*, 175739.
(67) Sivakumar, M.; Sidharth, D.; Srinivasan, B.; Arivanandhan, M. Improving thermoelectric performance of Nickel substituted ZnSb alloy through carrier engineering and nanostructuring. *J. Alloy. Compd.* **2024**, *1009*, 176908.

https://doi.org/10.1021/acsami.4c21670
ACS Appl. Mater. Interfaces 2025, 17, 17036−17044